UCSF

UC San Francisco Previously Published Works

Authors

Omene, Coral
Ma, Lin
Moore, Jade
et al.

Aggressive Mammary Cancers Lacking Lymphocytic Infiltration Arise in Irradiated Mice and Can be Prevented by Dietary Intervention

Coral Omene[1,*], **Lin Ma**[2,*], **Jade Moore**[2], **Haoxu Ouyang**[3], **Irineu Illa-Bochaca**[3], **William Chou**[2], **Manan S. Patel**[3], **Christopher Sebastiano**[3], **Sandra Demaria**[3,4], **Jian-Hua Mao**[5], **Kubra Karagoz**[1], **Michael L. Gatza**[1], **Mary Helen Barcellos-Hoff**[2,+]

[1]Rutgers Cancer Institute of New Jersey, Rutgers, The State University of New Jersey, New Brunswick, NJ

[2]University of California, San Francisco, San Francisco, CA

[3]New York University School of Medicine, New York, NY

[4]<u>Current address:</u> Department of Radiation Oncology, Weil Cornell Medical College, New York, NY

[5]Lawrence Berkeley National Laboratory, Berkeley, CA

Abstract

Because the incidence of breast cancer increases decades after ionizing radiation exposure, aging has been implicated in the evolution of the tumor microenvironment and tumor progression. Here, we investigated radiation-induced carcinogenesis using a model in which the mammary glands of 10-month-old BALB/c mice were transplanted with *Trp53*-null mammary tissue three days after exposure to low doses of sparsely ionizing γ-radiation or densely ionizing particle radiation. Mammary transplants in aged irradiated hosts gave rise to significantly more tumors that grew more rapidly than those in sham-irradiated mice, with the most pronounced effects seen in mice irradiated with densely ionizing particle radiation. Tumor transcriptomes identified a characteristic immune signature of these aggressive cancers. Consistent with this, fast-growing tumors exhibited an immunosuppressive tumor microenvironment with few infiltrating lymphocytes, abundant immunosuppressive myeloid cells, and high cyclooxygenase-2 and TGFβ. Only aged irradiated hosts gave rise to tumors lacking cytotoxic CD8^{+} lymphocytes (defined here as immune desert),

which also occurred in younger mice. These data suggested that host irradiation may promote immunosuppression. To test this, young chimera mice were fed chow containing a honeybee-derived compound with anti-inflammatory and immunomodulatory properties, caffeic acid phenethyl ester (CAPE). CAPE prevented the detrimental effects of host irradiation on tumor growth rate, immune signature, and immunosuppression. These data indicated that low-dose radiation, particularly densely ionizing radiation, promoted more aggressive cancers by suppressing antitumor immunity. Dietary intervention with a non-toxic immunomodulatory agent could prevent systemic effects of radiation that fuel carcinogenesis, supporting the potential of this strategy for cancer prevention.

Keywords

breast cancer; carcinogenesis; ionizing radiation; mouse models; inflammation

Introduction

The transformation of normal tissue into malignant cancer occurs under the influence of antitumor immunity and aging, both of which are key players in disease progression (1). Cancer evolution is also impacted by life-style, environment, and occupational exposures. In humans exposed to ionizing radiation, the period between exposure and increased risk of breast cancer is 30–40 years (2), hence host biology over decades likely modulates the evolution of biological features of a tumor that mediate its clinical behavior.

Radiation perturbs tissue homeostasis, in part, by activating inflammatory processes that may not resolve, leading to a cycle of subclinical tissue damage and chronic, low-level inflammation (3,4). Whereas one body of work clearly establishes the capacity of chronic inflammation to initiate and promote cancer (4), other studies show that an intact immune system can prevent, control, and shape cancer by a process known as 'cancer immunoediting' described by Mittal et al. (5). Because immune cells eliminate aberrant cells, this process of editing shapes the developing cancer and can ultimately promote escape of effective immune control (6). Importantly, pro-tumorigenic inflammation co-exists with antitumor immunity, and interventions that alter the balance in favor of one can either accelerate or hinder tumor growth (4).

Data from human and experimental models support the idea that interaction between intrinsic factors, such as host biology, and extrinsic conditions, including radiation exposure, significantly impact the biology of breast cancer. It is estimated that 8% of second primary cancers in the United States are associated with radiotherapy for first cancers in adults (7). Of concern are children who have been successfully treated with radiotherapy for childhood cancer. Women treated with radiation for a childhood cancer have a similar cumulative incidence of breast cancer by age 40 compared to women with *BRCA* gene mutations, and an incidence 10–20 times higher than the 1% cumulative incidence of general population (8). Compared to childhood cancer survivors who did not receive radiotherapy, girls treated with radiotherapy have a 2.9 higher relative risk of subsequently developing breast cancer, which is greater than that of women who are *BRCA* mutation carriers (9). Studies associate

childhood radiation treatment with more aggressive triple-negative breast cancer compared to age matched, spontaneous cancer controls (10,11).

Cancer incidence in humans increases exponentially with age, with 75% of newly diagnosed cases occurring in populations aged 55 years or older (https://www.cancer.gov/about-cancer/causes-prevention/risk/age). Aging is associated with low levels of chronic inflammation that may contribute to age-associated diseases, including cancer. Likewise, irradiation may increase inflammation. For example, serum IL6 increases both in older individuals (12) and atomic bomb survivors (13). Radiation exposure may also accelerate aging at some level (14). Modulating inflammation after irradiation is a prospective and achievable cancer prevention strategy in medically or occupationally irradiated populations that has not been tested.

We developed a radiation-genetic mammary chimera model to evaluate how carcinogenesis is affected by radiation-induced, non-mutational processes. Here, we examined the relationship between tumor microenvironment (TME) components and breast cancer phenotypes arising from *Trp53*-null mammary chimeras as a function of two factors, radiation type and host age. Densely ionizing radiation (DIR), which is present in the space radiation environment and used in radiation oncology, has potentially greater carcinogenic effect compared to sparsely ionizing radiation (SIR) that is prevalent on earth. Because occupational exposure (e.g. astronauts) and most radiotherapy occur in adults, here, we considered age at exposure as a factor. Compared to our prior studies in 10 week-old mice (15), the effect of radiation quality was greater in aged mice (10 months old), demonstrating that DIR was more effective than SIR at inducing aggressive tumors. However, tumors arising in both DIR- and SIR-irradiated hosts were characterized by rapid growth rate and an immunosuppressive TME, both of which we have previously reported in young mice (15,16). Only tumors arising in irradiated mice were devoid of lymphocytic infiltrates, suggesting that non-mutational, radiation effects promoted immune evasion. This prompted us to use caffeic acid phenethyl ester (CAPE), the major active component in propolis, a honeybee product that possesses immunomodulatory (anti-inflammatory) and anti-cancer properties (17). CAPE administered post-radiation in the diet of 10-week old mice prevented establishment of aggressive tumors with an immunosuppressive TME. These studies suggest that systemic inflammation and erosion of antitumor immunity elicited by radiation can be targeted after exposure to prevent aggressive tumors.

Materials and Methods

Animals

All animal experiments were performed at New York University School of Medicine (NYUSOM). The protocols for animal husbandry and experiments were conducted with institutional review and approval. 3-week old BALB/c mice that served as hosts were purchased from Jackson Laboratory (Bar Harbor, Maine). Syngeneic *Trp53*$^{-/-}$ BALB/c mice were bred as previously described to 8–10 week of age to provide donor mammary gland that was cryogenically preserved in 10% DMSO (16). All mice were housed 5 per cage, fed with Labdiet #5001 Rodent Formula (Purina Animal Nutrition LLC, St. Louis MO) and water *ad libitum*. The radiation-genetic chimera model was as previously described in which

the endogenous mammary epithelium of inguinal glands were surgically removed from 3-week-old wildtype BALB/c mice, the mice were aged prior to irradiation, and the inguinal fatpads subsequently transplanted with the *Trp53*^{-/-} donor mammary fragments (15,16).

For radiation quality experiments, mice aged to 10 months at NYUSOM were transported to Brookhaven National Laboratory (Upton, New York), which conducted institutional review and approval. Mice were acclimated for at least one week, and whole-body irradiation was performed at the NASA Space Radiation Laboratory in Brookhaven National Laboratory using a 5600 Curie (207 TBq) ^{137}Cs source to deliver sparsely ionizing radiation (SIR) to total body doses of 10, 50, or 100 cGy. Alternatively, mice were irradiated with densely ionizing radiation (DIR) using 600 MeV/amu Fe, 350 MeV/amu Ar, and 350 MeV/amu Si ions at equivalent fluences (3 particles per 10^2 mm) in which total body average doses were calculated to be 80 cGy for Fe, 49 cGy for Ar, and 30 cGy for Si. Contemporaneous controls were transported, anesthetized, and sham-irradiated. Three days after irradiation, the cleared mammary fat pads of host mice were transplanted with *Trp53*-null mammary gland fragments from non-irradiated donor mice. The approximately 1 mm^3 fragment was rapidly thawed from cryogenically preserved fragments of 8 to 10-week-old *Trp53*^{-/-} mice inguinal glands. Mice were transported to NYUSOM and quarantined for 6 weeks upon return. Mice were monitored by palpation at weekly intervals before 6 months, and twice weekly thereafter for 600 days post-transplantation.

For experiments using CAPE, BALB/c mice that served as hosts were purchased from Taconic Laboratory (Germantown, NY). The inguinal mammary glands of 3-week-old mice were cleared bilaterally of endogenous epithelium, as above. At 10–12 weeks old, the mice were irradiated with 100 cGy γ-rays or sham-irradiated at NYUSOM. The cleared mammary fat pads of host mice were transplanted with *Trp53*-null mammary gland fragments from non-irradiated donor mice 3 days later. Sham or irradiated mice were then randomly assigned to receive *ad libitum*, either control diet (7012 meal) containing caffeic acid phenethyl ester (CAPE) or control of 1% sucrose (Harlan Laboratories, Teklab lab animal diets, Madison, WI). CAPE was added in sucrose at 10 g/kg as 10 nmol diet (CAPE at 0.47 mg/kg), 500 nmol (CAPE at 23.5mg/kg), and 1000 nmol diet (CAPE at 47mg/kg). The CAPE concentration in the food and average food intake was used to estimate the dose. New 25 kg batches of diet were made every 3 months across the experiment. Blue or red food dyes at 0.2 g/kg diet were used to color code diets and prevent accidental feeding with the wrong diet. To preclude potential toxicity, dosing was escalated beginning with 10 nmol/mouse/day from 4 weeks after transplant until 14 weeks, increased to 500 nmol at 26 weeks and ending at 1000 nmol begun at 38 weeks, which was maintained for the remaining duration of the experiment. No toxicity (e.g. weight loss, poor grooming) was evident at any dose.

For all experiments, mice were palpated twice weekly from 6 months post transplantation. Palpable tumors were measured twice a week using calipers. Tumors reaching 1 cm^3 were resected using survival surgery. The resected tumor was divided into four portions. One portion was frozen in liquid nitrogen for RNA extraction, one portion was embedded in optimum cutting temperature (OCT) compound, one portion was formalin-fixed followed by paraffin embedding, and one portion was cut into fragments for viable preservation in

Dulbeco's Modified Eagle's Medium (DMEM) (Gibco, #10564–011) with 10% fetal bovine serum (Hyclone, #SH3007103) and 10% DMSO (Sigma, #D2650). Mice were further observed, and if the contralateral fat pad developed another tumor, then the tumor was monitored as above. If the resected tumor recurred, it was resected, and the mouse was euthanized. A gross necroscopy was performed upon termination. If no tumor developed from transplanted glands by the end of the experiment, mammary glands were collected, and the tissue stained by carmin alum (2g carmin from Sigma #1022; 2.5 aluminum potassium sulfate from Sigma #A-7167; and 0.05g thymol crystals from Sigma #T-0501 in 500 ml distilled water). The stained wholemounts were evaluated to ascertain successful transplantation. An informative transplant was defined as that which had an epithelial outgrowth evident by tumor development or >25% fat pad with gland development. Transplanted mammary glands that failed to develop epithelial outgrowths were censored.

Tumor growth rate analysis

Palpable tumors were measured twice weekly using calipers until reaching approximately 1 cm^3. Tumor volumes [V = (4/3) × π × (W/2) × (W/2) × (L/2)] of individual *Trp53*-null tumors were calculated for each measurement, and the growth rate fitted as an exponential curve Y=B*e^{AX} using all measurements where Y is the tumor volume at day X, A is the slope of the growth curve and B is the starting measure point of the tumor volume. To define fast versus slow tumor growth rate, the slopes of all tumor growth curves (n=33) were pooled, and the top quartile was designated as fast-growing (n=8) and the bottom quartile was designated as slow-growing (n=8).

Immunofluorescence

FFPE sections were dewaxed and rehydrated. Antigen retrieval was performed by using Antigen Unmasking Solution (Vector Laboratories, #H-3300) according to manufacturer instructions. The slides were then washed once with PBS and blocked with 0.5% casein (Spectrum, #CA205)/PBS for 1 hour at room temperature. Slides were incubated overnight at 4°C with 100 μl primary antibody against the indicated antigen diluted in blocking buffer (0.5% casein/PBS) as indicated: estrogen receptor (NCL-ER-6F11, Novocastra)(1:50) diluted in Superblock Blocking Buffer (Pierce, #37515), cleaved caspase 3 (9661S, Cell Signaling)(1:100), and COX-2 (ab15191, Abcam)(1:200). After washing with 0.1% Tween 20/PBS, slides were incubated for 1 hour at room temperature with 100 μl fluorochrome-conjugated secondary antibody dilutions (1:200 diluted in blocking buffer) of Alex Fluor-488-conjugated Donkey anti-mouse (Invitrogen #A21202) for recognizing ER; Alex Fluor-594-conjugated Donkey anti-rabbit (Invitrogen #A21207) for recognizing cleaved-caspase 3 and COX-2. Nuclei were counterstained with 4', 6-diamidino-2-phenylindole (DAPI, 2 mg/mL; Molecular Probes). Sections were washed in PBS before mounting with Vectashield mounting medium (Vector Labs). Specimens were imaged using a 20X Zeiss Plan-Apochromat objective with 0.95 numerical aperture on a Zeiss Axiovert epifluorescent microscope. All images were acquired with a CCD Hamamatsu Photonics monochrome camera at 1392 X 1040-pixel size, 12 bits per pixel depth. All images were assembled as false-color images using the Metamorph imaging platform (Molecular Devices, Inc.). Allred scoring was used to determine ER status (18). Cleaved caspase 3 was counted manually by positive cells per high powered field (HPF), and the mean calculated by counting five non-

overlapping random HPF sections per tumor. COX-2 intensity per HPF was measured using Fiji-Image J (NIH, Bethesda, MA) scripts.

Some antigens were analyzed using 5 μm cryosections from tumors frozen in O.C.T. (Sakura Tissue-Tek). Cryosections were fixed using 4% paraformaldehyde for 20 minutes at room temperature, specimens were blocked with 0.5% casein/PBS for 1 hour, and incubated with 100 μl anti-CD11b (ab75476, abcam)(1:200) and anti-Gr1 (MAB1037, R&D)(1:50) diluted in blocking buffer overnight at 4° C, followed by washes with 0.1% Tween 20/PBS and incubation with 100 μl Alexa Fluor-594 Donkey anti-rat (1:200)(Invitrogen #A21209) and Alexa Fluor-488 Donkey-anti-rabbit (1:200)(Invitrogen #A21206) secondary antibodies diluted in blocking buffer for 1 hour at room temperature. Specimens were counter-stained with DAPI and washed in PBS before mounting with Vectashield mounting medium. Specimens were imaged as described above. CD11b^{+}Gr1^{+} double-positive cells were counted manually per HPF, and the mean calculated by counting five non-overlapping random HPF sections per tumor.

OPAL Multiplex

FFPE sections were de-paraffinized and rehydrated before antigen unmasking by Antigen Unmasking Solution (Vector Laboratories, #H-3300 or #H-3301) according to manufacturer instructions. Endogenous peroxidase of each section was quenched by 100 μl 3% H_2O_2 in PBS (Diluted from 30% H_2O_2, Sigma #H1009) for 15 minutes and washed twice with TN buffer (0.1 M Tris-HCl, 0.15 M NaCl). The Opal 6-color kit (NEL796001KT, PerkinElmer) and Opal 7-color kit (NEL811001KT, PerkinElmer) were used. Each section passed through five or six sequential rounds of staining. Each round consisted of a protein block with 0.5% casein in TN buffer for 1 hour at room temperature, a primary antibody overnight incubation at 4°C, a corresponding secondary HRP-conjugated polymer incubation for 1 hour at room temperature, and a 10-minute incubation for each HRP-conjugated polymer, which mediated the covalent binding of a different fluorophore using tyramide signal amplification (all primary and secondary antibodies listed in Table 1). An additional antigen retrieval using heated citric acid buffer (pH 6.0) for 15 minutes was then used to remove bound antibodies before the next step in the sequence. After all sequential reactions, sections were counterstained with spectrum appropriate DAPI (NEL796001KT or NEL811001KT, PerkinElmer) and mounted with Vectashield Hard Set mounting medium (H-1400, Vectashield).

Opal stained sections were imaged using the Vectra Multispectral Imaging System version 2 (PerkinElmer). Images were analyzed by inForm 2.1 (PerkinElmer). Single stained slides for each marker and associated fluorophore were used to establish the spectral library, which helped to separate the individual marker from the multiplexing image cube. For each marker, positive cells were determined based on the mean fluorescent intensity per case. The inForm 2.1 (PerkinElmer) trainable tissue segmentation algorithm (PerkinElmer) was used to segment tumor and stromal regions based on the markers and DAPI stained nuclear shape. The percentage of positive cells for each marker in the region designated tumor or stroma were analyzed separately by the score algorithm (PerkinElmer) in 10 random images at 20× magnification.

Lymphocyte infiltrate pattern analysis

FFPE tumor sections were stained by CD8 (Table 1) as the method indicated above (Opal) and scanned using the Vectra system (PerkinElmer). The images of the whole sections were used for pattern analysis. The CD8^{+} T-cell infiltration into tumors was classified into three patterns: infiltrated, excluded, or desert. We defined infiltrated tumors as those with dense CD8^{+} cells that were well distributed across the tumor; excluded tumors were characterized by a dense accumulation of CD8^{+} cells at the tumor edge; and desert tumors contained few CD8^{+} cells. Tumor sections were evaluated by two observers blind to the experimental group.

Gene expression profiling

Frozen tumor tissues (50 mg) were lysed in 1 mL TRIzol™ reagent and homogenized with Omni Tissue Homogenizer on medium setting for 30 seconds, then incubated 3 minutes in 0.2 mL chloroform, followed by centrifuging for 15 minutes at 12,000 x g at 4°C. The aqueous phase was transferred to a new tube and 0.5 mL isopropanol was added for 10 minutes. Samples were then centrifuged for 10 minutes at 12,000 x g at 4°C. The supernatant was discarded, and the white gel-like pellets were resuspended in 1 mL of 75 % ethanol. The samples were then vortexed briefly, then centrifuged for 5 minutes at 7500 x g at 4°C. The supernatant was discarded, and the RNA pellet air-dried for 5–10 minutes before resuspending in 30 μL of RNase-free water. The samples were incubated in a heat-block at 60°C for 15 minutes before determining total RNA quality (RIN > 7.0), and quantity was determined using an Agilent 2100 Bioanalyzer and Nanodrop ND-100. The Affymetrix mouse Genechip 2.0 ST arrays were used according to manufacturer's protocol (ThermoFisher, #902119) for tumors from aged (10-month old) mice. Gene expression data is archived in Gene Expression Omnibus (GEO) under accession number GSE126769. The raw data was background adjusted and quantile-normalized using the Robust Multichip Average (RMA) algorithm from the Bioconductor package oligo (19). Read and mapping quality was analyzed using R package affyQCReport (20). Analyses were performed using BRB-ArrayTools developed by Dr. Richard Simon and the BRB-ArrayTools Development Team (21). Intrinsic subtyping was completed using the PAM50 method developed by Dr. Charles Perou and colleagues at the University of North Carolina at Chapel Hill (22). Express RNA-sequencing was performed on tumors derived from CAPE- and control-treated, irradiated hosts using the TruSeq RNA Sample Preparation Guide Protocol by Illumina® (#15008136 A). Raw sequencing data were received in FASTQ format. Read mapping was performed using Tophat 2.0.9 against the mm10 human reference genome (23). The resulting BAM alignment files were processed using the HTSeq 0.6.1 python framework and respective mm10 GTF gene annotation, obtained from the University of California, Santa Cruz (UCSC) database. Subsequently, the Bioconductor package DESeq2 (3.2) was used to identify differentially expressed genes (DEGs)(24). This package provides statistics for determination of DEGs using a model based on the negative binomial distribution. Gene expression data from RNA sequencing data is archived on GEO under accession number GSE128930. For both the microarray and RNA sequencing data, statistically significant genes were determined using the Benjamini–Hochberg's method for controlling false discovery rate (FDR). Genes with an adjusted p value < 0.05 were determined to be differentially expressed.

Gene clustering was done using a Pearson correlation coefficient (PCC). Pathway analysis and subsequent predictions in each tissue were defined using the statistically significant genes with a fold-change 1.2 or (–1.2) comparing treated versus sham controls. Gene set enrichment analysis (GSEA) using the Molecular Signatures Database's (MSigDB) eight major collections of gene sets (i.e. H, and C1–C7) (25) with an FDR < 0.05 from the entire list of genes was performed. A WEB-based gene set analysis toolkit (WebGestalt) was used to complete functional enrichment and pathway analysis of significant genes across treatments (26,27). All heatmaps were generated using ggplot2 package available through R.

The mean expression of gene expression signatures of specific aspects of immune cell signaling was calculated for each sample (n=23) as previously reported (28–32). The Student T-test was used to assess pathway scores between treatment groups. Tumors from sham, CAPE, IR, and IR + CAPE treated animals were compared using a panel of 18 gene expression signatures; red indicates high signature score (relative to dataset median) while blue corresponds with low relative score. Assessments of human TNBC subtypes of *Trp53*-null tumors were assigned using the TNBC subtype tool (33).

Statistical analysis

To compare growth rate between IR and sham groups, each growth curve was fitted as an exponential curve to extrapolate tumor size for a period representing the 30 days, as previously reported (16). R-values of >0.9 indicated that this was a reliable representation of the growth trajectory, therefore, tumor sizes in a treatment group were averaged every day for 30 days, independent of when the tumor arose, to permit comparison of growth rates between treatment groups. The growth rate of tumors within a treatment group was compared by averaging these normalized growth curves. The statistical analysis for all experimental data was performed using Prism 7 (GraphPad) and IBM SPSS Statistics. Differences between treatment groups were determined using Students t-test or Mann–Whitney test as indicated. PCC was used to test correlation between two components (IBM SPSS). A statistically significant difference was considered when p value was smaller than 0.05.

Results

Host age and radiation quality affects the frequency and spectrum of *Trp53*-null carcinomas

The radiation-genetic mammary chimera model separates non-mutational radiation effects and host biology, like age, that can influence cancer development. After the mice were irradiated, cleared mammary fat pads of mice aged to 10 months, which is roughly equivalent to a 45-year-old human, were transplanted with non-irradiated *Trp53*-null mammary epithelium (34) (Fig. 1A). We observed that only 50% of *Trp53* transplants generated outgrowths in aged mice, which is in contrast to our previous observation of 90% outgrowth efficiency in 10-week old mice (15,16), which is likely due to ovarian hormone decline. The reduced number of informative fat pads precluded statistically meaningful evaluation of radiation dose dependence. Therefore, mice were grouped according to radiation quality (i.e. SIR vs. DIR) for comparison to sham-irradiated mice.

The mean time to a palpable tumor was not affected by host irradiation (358±99 days for sham-hosts, n=7; 366±64 days for SIR-irradiated hosts, n=18; 353±76 days for DIR-irradiated hosts, n=27). However, the frequency of tumors arising from transplants in irradiated hosts was significantly increased compared to transplants in sham-irradiated contemporaneous controls (p<0.05, Chi-square)(Fig. 1B). Host irradiation with DIR was more effective than SIR in promoting tumorigenesis. Tumors arose from 20% of informative transplant outgrowths in sham-irradiated mice, 40% in mice exposed to SIR, and nearly 60% in mice exposed to DIR (Fig. 1B). Compared to our prior studies in mice irradiated at 10 weeks old (15,16,35), the differential between sham and irradiated hosts at 10 months was greater, as was the differential between SIR and DIR.

The murine mammary gland consists of two major cell types, basal myoepithelial cells that express keratin 14 (K14) and p63, and luminal cells that express keratin 8/18 (K18) and estrogen receptor (ER). Most (60%) cancers arising from *Trp53*-null outgrowths in young mice (10 weeks at transplant) are ER-positive, which host irradiation decreases (16,36). Compared to young mice, fewer (33%, 3/9) ER-positive cancers arose in aged, sham-irradiated mice. The frequency was similar (39%, 5/13) for tumors arising in SIR-irradiated aged hosts but was decreased in DIR-irradiated mice (21%, 5/24)(Fig. 1C). In young mice, most *Trp53*-null tumors arising in sham-irradiated hosts exhibit a pseudo-glandular pattern consisting of K14- and K18-positive cells, whereas either SIR or DIR host irradiation favors K18 tumors (15). In aged mice, nearly half of the tumors were negative for both keratins (Fig. 1D). Compared to tumors arising in sham-irradiated aged hosts, SIR or DIR host irradiation favored development of pseudo-glandular tumors (i.e. K14/K18) at the expense of K18 tumors. These data extend our prior work showing that SIR and DIR exposure affects the tumor spectrum arising from non-irradiated *Trp53*-null epithelium (29).

Host irradiation leads to rapid growth of subsequent tumors

The growth rate of individual *Trp53*-null tumors is heterogeneous, but tumors arising in irradiated young mice consistently grow faster, regardless of latency (15,16,35,36). To permit comparison among tumors, each growth curve within a treatment group was fitted as an exponential curve, which was used to extrapolate tumor size for a period of 30 days post-detection, independent of when the tumor arose. The growth rate of tumors arising in aged mice irradiated with either SIR or DIR was significantly faster than tumors arising in aged sham-irradiated mice (p=0.003; Fig. 1E). Because we previously reported this phenotype in young irradiated mice (15,16), the data suggest that rapid growth rate is a consequence of host irradiation rather than host age *per se*, although older age appears to exacerbate the effect of host irradiation.

Tumor growth rate is the sum of cell production and loss. Tumor cell mitotic rate was not different between treatment groups (23±3 for sham hosts, n=9; 25±6 for SIR hosts, n=16; 23±2, n=26 for DIR hosts), nor was proliferation rate as marked by Ki67 (20%±4% for sham hosts, n=8; 16%±3% for SIR hosts, n=7; 16%±3%, n=13 for DIR hosts). We next tested cell loss using cleaved caspase 3, a marker of apoptotic cells. Apoptosis was significantly greater in tumors arising in sham-irradiated versus irradiated hosts (p=0.02; Fig. 1F).

Tumors arising in irradiated host exhibit distinct expression signatures

To explore how host irradiation globally impacted tumor features that mediate growth, we used an Affymetrix Genechip™ Mouse Gene 2.0 ST platform to profile RNA of 43 tumors arising in sham (n=9), SIR (n=15), and DIR (n=19) irradiated, aged mice. Of these, 32 tumors were ER-negative and 11 were ER-positive. Mammary cancers arising from *Trp53*-null epithelium are genomically heterogeneous in a manner that reflects the diversity of human breast cancers (35,37,38). Using PAM50-based molecular subtyping (22), we assessed the distribution of intrinsic breast cancer subtypes (Supplementary Fig. S1A). The overall subtype distribution was 42% luminal A (18/43), 21% luminal B (9/43), 12% HER2-enriched (5/43), 16% basal-like (7/43), and 9% normal-like (4/43)(Supplementary Fig. S1B). Among ER-positive tumors, 45% were categorized as luminal A by PAM50 (Supplementary Fig. S1C). The spectrum of PAM50-intrinsic subtypes was significantly affected by DIR host irradiation but not by SIR host irradiation ($p<0.05$, ANOVA).

Unsupervised hierarchical clustering (UHC) of all genes identified three tumor clades distinguished by five major gene clusters (Fig. 2A). Group 1 (G1) was composed of nine tumors arising only in irradiated hosts, the majority of which (6/9) were from DIR-exposed mice. Group 2 (G2; n=16) contained mostly (6/9) tumors arising in sham-irradiated mice. Group 3 (G3; n=18) was composed of tumors from all treatments but mostly included (8/15) tumors arising in SIR-irradiated hosts. Tumor ER status did not appear to be a factor, as it was distributed across groups. The five major gene clusters were found to be overrepresented by gene set enrichment analysis (25). These clusters represented significant differences among tumors and showed downregulation of genes associated with mammary stem cells (cluster 1), immune system processes (cluster 2), cellular response to external stimulus (cluster 3), epithelial to mesenchymal transition, and transforming growth factor beta (TGFβ)(cluster 4). A set of genes was also upregulated in mammary stem cells (cluster 5)(Supplementary Table S1). These processes were similar to those we identified for tumors arising in young, irradiated mice (15,16,36).

G1 expression profile patterns were the most distinctive. Two clusters of genes associated with mammary stem cells were low in G1 tumors compared to tumors in G2 and G3. G1 tumors were also characterized by genes decreased upon loss of E-cadherin, which promotes metastasis (39), and is caused by TGFβ activation, particularly in irradiated cells (40). G2 and G3 tumors expression profile patterns were more heterogeneous than G1 tumors. The G2 group was characterized by high expression of mammary stem cell genes, whereas G3 group expressed genes decreased in mammary stem cells, as well as genes associated with TGFβ. G1 tumors were characterized by *BMP2* activity, which is reported to affect progesterone receptor signaling and induction of prostaglandin synthase (41).

G1, which consisted entirely of tumors arising in irradiated mice, exhibited high expression of genes in the immune system processes cluster 2, which was further refined as 3 minor gene clusters that implicated discrete immune processes: leukocyte trafficking ($p<0.05$), apoptosis-related ($p<0.05$), and inflammatory processes ($p>0.001$)(Fig. 2B). In contrast, G2, which was enriched in tumors arising in sham-irradiated mice, exhibited low expression of gene cluster 2, whereas G3 tumors exhibited an intermediate pattern – genes associated with

leukocyte trafficking and inflammatory processes were elevated but apoptosis-related activities were reduced compared to G1.

Specific genes were enriched in G1 tumors compared to tumors in G2 and G3 (Supplemental Table S2). Leukocyte endogenous mediators included a 17-fold increase in *Il1b*, as well as anti-apoptotic *Xiap* (x-linked inhibitor of apoptosis protein) and *Bir* (*Baculovirus* inhibitor of apoptosis protein repeat). Key pro-inflammatory mediators included a 16-fold change in *Ptgs2*, which encodes cyclooxygenase-2 (COX-2). Expression of *Ptgs2* was significantly elevated in tumors arising in irradiated hosts (Fig. 3A). Thus, programs important in immunity and inflammation distinguished tumors arising in irradiated hosts from those arising in sham-irradiated hosts.

To further test this idea, we then conducted supervised comparison of ER-negative tumors using 725 cluster 2 genes implicated in immune functions (Supplementary Table S3). Expression profiling of tumors arising in irradiated versus sham-irradiated hosts indicated that genes involved in inflammatory and immune response (21 genes), extracellular matrix disassembly (18 genes), and immune cell trafficking (32 genes) were the top-ranked ($p > 0.001$) processes that distinguished tumors from irradiated aged mice from sham-irradiated mice. Among the 15 most significant upstream regulators identified by DAVID (the database for annotation, visualization, and integrated discovery) ranked by z-score ($p < 0.05$), the majority were pro-inflammatory factors, including IL4, IL4 receptor, IL1β, and TGFβ. Our previous work showed that TGFβ is a critical signal in the irradiated host (16,36,38).

Among the top ranked upregulated molecules were COX-2 and granzyme D. We sought to confirm *Ptgs2* gene expression, whose product is COX-2, by assessing COX-2 protein via immunofluorescence (Fig. 3B). Tumors from irradiated hosts exhibited increased COX-2 immunostaining compared to tumors from sham-irradiated mice. COX-2 promotes the immunosuppressive activity of myeloid-derived suppressor cells and tumorigenesis (42). Thus, we sought validation of COX-2 activity by enumerating CD11b^{+}Gr1^{+} cells, which were increased in tumors from irradiated host (Fig. 3C). These cells bared the markers of suppressive myeloid cells, some of which might harbor suppressive activity, and could also reflect neutrophils that are known to be suppressive in some contexts. Further phenotypic experiments are needed to determine if this population is functionally immunosuppressive. The frequency of CD11b^{+}Gr1+ cells was positively correlated with COX-2 intensity (PCC r = 0.48, $p < 0.05$)(Fig. 3D). Together with the accelerated growth rate, these data led us to investigate the tumor immune infiltrate as a function of host irradiation.

The pattern of immune infiltrates of tumors arising in irradiated aged mice is distinct

Inflamed tumors exhibit pre-existing immunity, as evidenced by an abundance of tumor-infiltrating lymphocytes (TILs) and expression of checkpoint markers including PD-L1. Tumors that exclude T cells often exhibit immunosuppressive immune cells, reactive stroma, and angiogenesis. A third class of tumors are devoid of significant T-cell infiltrate, i.e. deserts, which are generally genomically stable and proliferative (43). We classified tumors according to CD8^{+} TIL patterns (Fig. 4A). Tumors arising in sham-irradiated mice (n=8) were either infiltrated (63%) or excluded (37%). In contrast, 28% (n=43) of tumors arising

in irradiated mice were deserts. Quantitative analysis using InForm™ software to enumerate the percentage of CD8$^+$ T cells in tumor versus stroma showed that CD8$^+$ T-cell frequency in the tumor, but not the stroma, was significantly lower in tumors from irradiated hosts (Fig. 4B).

Tumor cell apoptosis from cytotoxic T-cell activation can limit tumor growth by both direct and indirect mechanisms (44). Consistent with functional, though ineffective, antitumor immunity, the frequency of CD8$^+$ TILs negatively correlated with tumor growth rate (Fig. 4C) and COX-2 expression (Fig. 4D). To facilitate analysis of the biology associated with tumor growth rate, tumors (n=33) were divided into quartiles based on growth. The top quartile was designated as fast-growing (n=8) and the bottom quartile were designated as slow-growing (n=8). More tumors in the fast-growing group were deserts or excluded than in the slow-growing group (Fig. 4E). Exclusion of lymphocytes is often accompanied by high prevalence of myeloid cells (45,46). We found that the frequency of CD11b$^+$Ly6G$^+$ cells was greater in fast-growing tumors (Fig. 4F) and positively correlated with growth rate across all tumors (Fig. 4G). Ineffective antitumor immunity could also be due to PD-L1 expression (47), and COX-2 regulates PD-L1 expression in tumor-associated macrophages (48). Consistent with this, PD-L1 expression was increased in fast-growing tumors (Fig. 4H).

We next considered the TGFβ gene signature that characterized tumors arising in the irradiated aged host. Radiation induces acute TGFβ activation, whose effects are persistent (16,36). TGFβ is known for its ability to suppress lytic activity of CD8$^+$ T-cell function (45) and is a key signal that promotes immunosuppressive myeloid differentiation and their efficacy in suppressing cytolytic lymphocytes (49). Hence, we evaluated immunostaining of active TGFβ (Fig. 4I) and phosphorylation of SMAD2 (pSMAD2), the downstream target of TGFβ receptor kinase (Fig. 4J), which were both significantly increased in fast-growing tumors, consistent with a role of TGFβ as a key component of the immunosuppressive TME. Together, unsupervised genomic analysis and validation immunostaining indicated that host irradiation promoted tumors with an immunosuppressive TME in which high TGFβ and pronounced myeloid infiltration likely leads to exclusion of CD8$^+$ lymphocytes and aggressive tumor behavior.

Dietary CAPE prevents the irradiated host tumor phenotype

Advanced host age at irradiation increased *Trp53*-null tumor frequency, but rapid tumor growth rate is also observed in *Trp53*-null carcinomas arising in young (10-week) irradiated hosts (15,16,35,36). Both radiation and aging are associated with decreased immunity and increased inflammation (13,50). To test whether modulating inflammation early in carcinogenesis affected the tumor type that developed, we conducted experiments with young mice. Mammary glands were cleared at 3 weeks, mice were irradiated (100 cGy γ-radiation) at 10 weeks and were transplanted with *Trp53*-null mammary fragments three days later (Fig. 5A). Mice were randomized 30 days later to chow containing CAPE, a non-toxic, anti-inflammatory compound (major active component of honeybee propolis) that has demonstrated anti-cancer and immunomodulatory properties (17). We chose CAPE primarily because of its natural favorable toxicity profile, which makes it an attractive

potential treatment in humans, and because our work using CAPE demonstrates its anti-proliferative effects on breast cancer (51,52).

The time course of tumor detection was statistically different (p<0.01) among irradiated hosts compared to sham-irradiated hosts (Fig. 5B). Similar to the effect of aged host irradiation on tumor growth rate described above (Fig. 1), tumors arising in young, irradiated, control chow–fed hosts grew significantly faster than those arising in sham-irradiated hosts (Fig. 5C). Tumors arising in CAPE-fed mice exhibited a growth rate similar to sham-irradiated mice on control diet (Fig. 5C). The pattern of CD8$^+$ TILs from tumors arising irradiated, control chow–fed mice were similar to aged mice and included 30% classified as deserts (Fig. 5D). In contrast, tumors from irradiated mice on the CAPE-diet were predominantly infiltrated (80%), like the distribution obtained in sham-irradiated hosts.

We then examined the TME associated with tumors arising in irradiated hosts. CAPE inhibits the release of arachidonic acid from cell membranes, suppresses the enzyme activities of COX-1 and COX-2, and decreases COX-2 gene expression (53). Tumors from irradiated mice treated with CAPE exhibited decreased COX-2 (Fig. 6A), PD-L1$^+$ cells (Fig. 6B), and CD11b$^+$GR1$^+$ myeloid cells (Fig. 6C). In contrast, CD8$^+$ TILs increased (Fig. 6D). Consistent with host irradiation acting via TGFβ, tumors arising in irradiated CAPE-treated mice exhibited low TGFβ and pSMAD2 (Fig. 6E–F). The altered immune composition of tumors arising in CAPE-treated, irradiated hosts was accompanied by increased apoptosis (Fig. 6G), concordant with their decreased growth rate compared to tumors arising in irradiated mice.

We next conducted RNA sequencing (RNA-Seq) of ER-negative tumors. We first sought to determine whether *Trp53*-null ER-negative tumors reflected the subtypes of human triple-negative breast cancer (TNBC)(54), using the TNBC type tool to assign subtype (33). We found that the subtypes of human TNBC were reflected in the spectrum of *Trp53*-null tumors. Although TNBC subtype distribution varied by host treatment, the spectrum was not significantly different among treatment groups (Supplementary Fig. S2).

We then applied the immune gene expression cluster 2 (725 genes) identified from the microarray data (Fig. 6H). Tumors arising in irradiated mice clustered exclusively together in one arm of the dendrogram compared to tumors arising in sham, CAPE-treated and CAPE-treated, irradiated mice. Tumors arising in irradiated mice exhibited reduced cytokine and chemokine signaling necessary for antigen-presenting cell and T-cell migration and recruitment, as well as leukocyte activation. In comparison, tumors arising in CAPE-treated, irradiated mice were characterized by a significant reduction in overall inflammatory signaling and greater expression of antigen processing and presentation and leukocyte trafficking genes. To further assess these data, we examined a panel of previously published gene expression signatures that have been shown to measure aspects of immune signaling (28–32). These analyses demonstrated altered expression of both adaptive and innate immunity across treatment cohorts. Host irradiation resulted in tumors characterized by reduction (p<0.05) of multiple signatures including T cells and T cell–associated signatures (CD8, IL8, LCK), macrophages and macrophage-associated signatures (CD68, MφTh1, MφCSF1, HCK), as well as neutrophil and natural killer cell signatures (CD44 and CD56)

relative to sham-treated tumors (Fig. 6I, Supplementary Table S4). This shift in immune signaling was rescued by CAPE treatment of irradiated animals to levels present in tumors arising in control mice. CAPE alone did not appear to influence immune signaling. These data support host irradiation *per se* as the primary instigator of the immunosuppressive TME. Thus, treating mice with a dietary anti-inflammatory agent after radiation exposure prevented the consequences of host irradiation that drives aggressive tumors and an immunosuppressive TME.

Discussion

Here we used a model of *de novo* mammary carcinogenesis to show that host exposure to DIR or SIR at 10 months of age, which is roughly equivalent to middle-age in humans, promoted aggressive breast cancer characterized by rapid growth, an immunosuppressive TME, and sparse tumor-infiltrating lymphocytes. DIR, considered to be a more effective carcinogen than SIR, was significantly more effective in aged mice, suggesting an unexpected synergy between age and radiation quality. We focused on understanding the basis for the pronounced non-targeted radiation effect on rapid tumor growth rate, which is also evident in young irradiated hosts (15,16). We found that only irradiated hosts gave rise to tumors lacking cytotoxic CD8$^+$ lymphocytes (i.e. immune deserts), and that the TME of fast-growing tumors was high in COX-2 and TGFβ. These data suggested the hypothesis that host irradiation promotes inflammation and compromises systemic immune surveillance. To test whether compromised tumor immunity could be rescued, young mice were fed chow supplemented with CAPE, an anti-inflammatory and immunomodulatory compound, after irradiation. Dietary CAPE prevented the development of rapidly growing, lymphocytic desert tumors, consistent with transcriptomic rewiring. These data suggest that non-mutational radiation effects, particularly from DIR, were exacerbated in aged mice to fuel development of aggressive cancers by repressing antitumor immunity.

Although the possibility of a radiation-induced oncogenic mutation is widely believed to be the critical mechanism of carcinogenesis (55), human and experimental animal data suggests radiation exposure may activate or augment a cycle of subclinical inflammation and low-level tissue damage. Meanwhile, during the protracted evolution of cancer, the immune system concomitantly deteriorates with age, evidenced by increased pro-inflammatory cytokines, including TGFβ, that are associated with increased risk of cancer (56,57). Our studies suggest that these interact to drive aggressive cancer, particularly following DIR.

Radiation affects cell phenotype and intercellular signaling that modify cell-cell interactions and the surrounding microenvironment, referred to as non-targeted effects (58). We developed the mammary chimera model to evaluate whether host biology after exposure to radiation affects carcinogenesis. This model separates the effect of radiation on initiation, presumably via DNA damage and mutation, from those non-mutational mechanisms that may act on promotion. Cancers arising from *Trp53*-null outgrowths a year or more after host irradiation are more frequently ER-negative and metastatic and consistently grow more rapidly once detected compared to those arising in sham-irradiated mice (15,16,36). To ascertain the genetic contribution to cancer development following radiation, mice resistant to cancer development were crossed to sensitive mice, then backcrossed to generate

genetically diverse mice that were used as hosts in the *Trp53*-null mammary chimera model (35). Bioinformatics analysis of the genetic loci associated with tumor latency in irradiated mice identified enrichment for genes involved in immune response, including signaling pathways of natural killer cells and cytokines. Consistent with this, plasma levels of certain cytokines in irradiated mice are significantly associated with tumor latency. Analysis of the candidate genes within these loci identified TGFβ as a critical upstream regulator in irradiated mice, consistent with our prior studies using $Tgfb1^{+/−}$ hosts (16). Our studies in aged mice confirmed the TGFβ signature.

Correlative analysis of the tumor phenotypes and TME showed that lack of lymphocytic infiltrate was associated with rapid tumor growth rate. Subsequent expression profiling and prior literature led to the hypothesis that low-dose radiation exposure compromises antitumor immunity, but the exact nature of the immune changes is insufficiently clear. Although cell type depletion studies could lend further support, our model, in which tumors arise after 12–18 months, makes this approach very challenging. Depletion of a specific cell type (e.g. CD4 or CD8) with specific antibodies to cell surface markers is widely used but would not be feasible for the duration of the experiment, nor can they be timed to coincide with a specific event because tumors arise spontaneously.

Dietary anti-inflammatory CAPE abrogated the effect of host irradiation that promoted aggressive tumors. CAPE inhibits cytokine and chemokine production, the proliferation of T cells, and lymphokine production. Thus, it suppresses the inflammatory process and is a potent and a specific inhibitor of nuclear factor-κB activation (17). Mechanistically, CAPE has been shown to exhibit its anti-inflammatory effects by being the most potent modulator of arachidonic acid cascade and through the inhibition of leukotriene production and prostaglandin formation by inhibiting cyclooxygenase and lipoxygenase pathways. COX-2 may be a critical factor in allowing cancer cells to escape host immune defenses by modulation of cytokine production, dysfunction of dendritic cells, and suppression of lymphocyte proliferation associated with immunosuppression and tumorigenesis (59). Consistent with this, COX-2 was significantly upregulated in tumors arising from irradiated hosts but when treated with CAPE, the suppressive immune signature was reversed, and COX-2 expression significantly decreased.

We observed an inverse relationship between COX-2 and $CD8^+$ T-cell infiltration, and high TILs is a favorable prognostic factor in certain breast cancer subtypes (60). COX-2 inhibition in mice accelerates accumulation of cytotoxic T cells within tumors and consequently slows tumor growth (61). Our data suggested that these cytotoxic TILs were reactive, albeit insufficient to eliminate tumors, as evidenced by slower tumor growth. COX-2 expression negatively correlated with TILs in fast-growing tumors, as was PD-L1, which was abrogated in CAPE-fed mice. CAPE treatment of irradiated hosts significantly decreased subsequent tumor growth rate and increased apoptosis, consistent with the observed increased TILs. CAPE treatment only affected these parameters in tumors arising from the irradiated hosts compared to sham-irradiated mice.

In conclusion, we showed that aged mice exposed to ionizing radiation drives mammary cancers that are more aggressive by repressing aspects of antitumor immunity resulting in an

immunosuppressive TME. Although radiation quality and age appear to particularly synergize, this biology was evident in young mice in which dietary intervention with CAPE mitigated radiation's systemic effects. The concept that establishment of an immunosuppressive TME fuels radiation carcinogenesis adds credence to the use of anti-inflammatory agents in breast cancer prevention. Further support is given to this idea by the current ongoing clinical trial using aspirin as an adjuvant therapy for breast cancer ().

Supplementary Material

Refer to Web version on PubMed Central for supplementary material.

Acknowledgments

References

1. Barcellos-Hoff MH, Lyden D, Wang TC. The evolution of the cancer niche during multistage carcinogenesis. Nat Rev Cancer 2013;13(7):511–8 doi 10.1038/nrc3536. [PubMed: 23760023]

2. Ronckers CM, Erdmann CA, Land CE. Radiation and breast cancer: a review of current evidence. Breast cancer research : BCR 2005;7:21–32. [PubMed: 15642178]

3. Medzhitov R. Inflammation 2010: New Adventures of an Old Flame. Cell 2010;140(6):771–6 doi 10.1016/j.cell.2010.03.006. [PubMed: 20303867]

4. Grivennikov SI, Greten FR, Karin M. Immunity, Inflammation, and Cancer. Cell 2010;140(6):883–99 doi 10.1016/j.cell.2010.01.025. [PubMed: 20303878]

5. Mittal D, Gubin MM, Schreiber RD, Smyth MJ. New insights into cancer immunoediting and its three component phases-elimination, equilibrium and escape. Curr Opin Immunol 2014;27C:16–25 doi 10.1016/j.coi.2014.01.004.

6. Schreiber RD, Old LJ, Smyth MJ. Cancer immunoediting: integrating immunity's roles in cancer suppression and promotion. Science (New York, NY) 2011;331(6024):1565–70 doi 10.1126/science.1203486.

7. Berrington de Gonzalez A, Curtis RE, Kry SF, Gilbert E, Lamart S, Berg CD, et al. Proportion of second cancers attributable to radiotherapy treatment in adults: a cohort study in the US SEER cancer registries. The Lancet Oncology 2011;12(4):353–60 doi 10.1016/S1470-2045(11)70061-4. [PubMed: 21454129]

8. Bhatia S, Robison LL, Oberlin O, Greenberg M, Bunin G, Fossati-Bellani F, et al. Breast cancer and other second neoplasms after childhood Hodgkin's disease. N Engl J Med 1996;334(12):745–51. [PubMed: 8592547]

9. Moskowitz CS, Chou JF, Wolden SL, Bernstein JL, Malhotra J, Novetsky Friedman D, et al. Breast cancer after chest radiation therapy for childhood cancer. Journal of clinical oncology : official journal of the American Society of Clinical Oncology 2014;32(21):2217–23 doi 10.1200/jco.2013.54.4601. [PubMed: 24752044]

10. Castiglioni F, Terenziani M, Carcangiu ML, Miliano R, Aiello P, Bertola L, et al. Radiation effects on development of HER2-positive breast carcinomas. Clin Cancer Res 2007;13(1):46–51 doi 10.1158/1078-0432.ccr-06-1490. [PubMed: 17200337]

11. Horst KC, Hancock SL, Ognibene G, Chen C, Advani RH, Rosenberg SA, et al. Histologic subtypes of breast cancer following radiotherapy for Hodgkin lymphoma. Annals of Oncology 2014;25(4):848–51 doi 10.1093/annonc/mdu017. [PubMed: 24608191]

12. Sarkar D, Fisher PB. Molecular mechanisms of aging-associated inflammation. Cancer letters 2006;236(1):13–23. [PubMed: 15978720]

13. Hayashi T, Kusunoki Y, Hakoda M, Morishita Y, Kubo Y, Maki M, et al. Radiation dose-dependent increases in inflammatory response markers in A-bomb survivors. International journal of radiation biology 2003;79(2):129–36. [PubMed: 12569016]

14. Harman D. Aging: a theory based on free radical and radiation chemistry. J Gerontol 1956;11(3): 298–300. [PubMed: 13332224]

15. Illa-Bochaca I, Ouyang H, Tang J, Sebastiano C, Mao J-H, Costes SV, et al. Densely Ionizing Radiation Acts via the Microenvironment to Promote Aggressive Trp53 Null Mammary Carcinomas. Cancer research 2014;74(23):7137–48 doi 10.1158/0008-5472.CAN-14-1212. [PubMed: 25304265]

16. Nguyen DH, Oketch-Rabah HA, Illa-Bochaca I, Geyer FC, Reis-Filho JS, Mao JH, et al. Radiation Acts on the Microenvironment to Affect Breast Carcinogenesis by Distinct Mechanisms that Decrease Cancer Latency and Affect Tumor Type. Cancer Cell 2011;19(5):640–51 doi 10.1016/j.ccr.2011.03.011. [PubMed: 21575864]

17. Armutcu F, Akyol S, Ustunsoy S, Turan FF. Therapeutic potential of caffeic acid phenethyl ester and its anti-inflammatory and immunomodulatory effects (Review). Experimental and therapeutic medicine 2015;9(5):1582–8 doi 10.3892/etm.2015.2346. [PubMed: 26136862]

18. Harvey JM, Clark GM, Osborne CK, Allred DC. Estrogen receptor status by immunohistochemistry is superior to the ligand-binding assay for predicting response to adjuvant endocrine therapy in breast cancer. Journal of clinical oncology : official journal of the American Society of Clinical Oncology 1999;17(5):1474–81. [PubMed: 10334533]

19. Carvalho BS, Irizarry RA. A framework for oligonucleotide microarray preprocessing. Bioinformatics 2010;26(19):2363–7 doi 10.1093/bioinformatics/btq431. [PubMed: 20688976]

20. Gautier L, Cope L, Bolstad BM, Irizarry RA. affy--analysis of Affymetrix GeneChip data at the probe level. Bioinformatics 2004;20(3):307–15 doi 10.1093/bioinformatics/btg405. [PubMed: 14960456]

21. Zhao Y, Simon R. BRB-ArrayTools Data Archive for human cancer gene expression: a unique and efficient data sharing resource. Cancer informatics 2008;6:9–15 doi 10.4137/cin.s448. [PubMed: 19259398]

22. Parker JS, Mullins M, Cheang MC, Leung S, Voduc D, Vickery T, et al. Supervised risk predictor of breast cancer based on intrinsic subtypes. Journal of clinical oncology : official journal of the American Society of Clinical Oncology 2009;27(8):1160–7 doi 10.1200/jco.2008.18.1370. [PubMed: 19204204]

23. Kim D, Pertea G, Trapnell C, Pimentel H, Kelley R, Salzberg SL. TopHat2: accurate alignment of transcriptomes in the presence of insertions, deletions and gene fusions. Genome biology 2013;14(4):R36 doi 10.1186/gb-2013-14-4-r36. [PubMed: 23618408]

24. Love MI, Huber W, Anders S. Moderated estimation of fold change and dispersion for RNA-seq data with DESeq2. Genome biology 2014;15(12):550 doi 10.1186/s13059-014-0550-8. [PubMed: 25516281]

25. Subramanian A, Tamayo P, Mootha VK, Mukherjee S, Ebert BL, Gillette MA, et al. Gene set enrichment analysis: a knowledge-based approach for interpreting genome-wide expression profiles. Proceedings of the National Academy of Sciences of the United States of America 2005;102(43):15545–50 doi 10.1073/pnas.0506580102. [PubMed: 16199517]

26. Zhang B, Kirov S, Snoddy J. WebGestalt: an integrated system for exploring gene sets in various biological contexts. Nucleic acids research 2005;33(Web Server issue):W741–8 doi 10.1093/nar/gki475. [PubMed: 15980575]

27. Wang J, Duncan D, Shi Z, Zhang B. WEB-based GEne SeT AnaLysis Toolkit (WebGestalt): update 2013. Nucleic acids research 2013;41(Web Server issue):W77–83 doi 10.1093/nar/gkt439. [PubMed: 23703215]

28. Iglesia MD, Parker JS, Hoadley KA, Serody JS, Perou CM, Vincent BG. Genomic Analysis of Immune Cell Infiltrates Across 11 Tumor Types. J Natl Cancer Inst 2016;108(11) doi 10.1093/jnci/djw144.

29. Bindea G, Mlecnik B, Tosolini M, Kirilovsky A, Waldner M, Obenauf AC, et al. Spatiotemporal dynamics of intratumoral immune cells reveal the immune landscape in human cancer. Immunity 2013;39(4):782–95 doi 10.1016/j.immuni.2013.10.003. [PubMed: 24138885]

30. Shipitsin M, Campbell LL, Argani P, Weremowicz S, Bloushtain-Qimron N, Yao J, et al. Molecular Definition of Breast Tumor Heterogeneity. Cancer Cell 2007;11(3):259–73. [PubMed: 17349583]

31. Yoshihara K, Shahmoradgoli M, Martinez E, Vegesna R, Kim H, Torres-Garcia W, et al. Inferring tumour purity and stromal and immune cell admixture from expression data. Nature communications 2013;4:2612 doi 10.1038/ncomms3612.

32. Fan C, Prat A, Parker JS, Liu Y, Carey LA, Troester MA, et al. Building prognostic models for breast cancer patients using clinical variables and hundreds of gene expression signatures. BMC Medical Genomics 2011;4(1):3 doi 10.1186/1755-8794-4-3. [PubMed: 21214954]

33. Chen X, Li J, Gray WH, Lehmann BD, Bauer JA, Shyr Y, et al. TNBCtype: A Subtyping Tool for Triple-Negative Breast Cancer. Cancer informatics 2012;11:147–56 doi 10.4137/cin.s9983. [PubMed: 22872785]

34. Jerry DJ, Kittrell FS, Kuperwasser C, Laucirica R, Dickinson ES, Bonilla PJ, et al. A mammary-specific model demonstrates the role of the p53 tumor suppressor gene in tumor development. Oncogene 2000;19(8):1052–8. [PubMed: 10713689]

35. Zhang P, Lo A, Huang Y, Huang G, Liang G, Mott J, et al. Identification of genetic loci that control mammary tumor susceptibility through the host microenvironment. Scientific reports 2015;5:8919 doi 10.1038/srep08919. [PubMed: 25747469]

36. Tang J, Fernandez-Garcia I, Vijayakumar S, Martinez-Ruiz H, Illa-Bochaca I, Nguyen DH, et al. Irradiation of juvenile, but not adult, mammary gland increases stem cell self-renewal and estrogen receptor negative tumors. Stem Cells 2013;32(3):649–61 doi 10.1002/stem.1533.

37. Herschkowitz JI, Simin K, Weigman VJ, Mikaelian I, Usary J, Hu Z, et al. Identification of conserved gene expression features between murine mammary carcinoma models and human breast tumors. Genome biology 2007;8(5):R76 doi gb-2007-8-5-r76 [pii] 10.1186/gb-2007-8-5-r76. [PubMed: 17493263]

38. Nguyen DH, Fredlund E, Zhao W, Perou CM, Balmain A, Mao J-H, et al. Murine Microenvironment Metaprofiles Associate with Human Cancer Etiology and Intrinsic Subtypes. Clin Cancer Research 2013;19(6):1353–62 doi 10.1158/1078-0432.ccr-12-3554.

39. Onder TT, Gupta PB, Mani SA, Yang J, Lander ES, Weinberg RA. Loss of E-Cadherin Promotes Metastasis via Multiple Downstream Transcriptional Pathways. Cancer research 2008;68(10):3645–54 doi 10.1158/0008-5472.can-07-2938. [PubMed: 18483246]

40. Andarawewa KL, Erickson AC, Chou WS, Costes SV, Gascard P, Mott JD, et al. Ionizing radiation predisposes nonmalignant human mammary epithelial cells to undergo transforming growth factor β induced epithelial to mesenchymal transition. Cancer research 2007;67:8662–70. [PubMed: 17875706]

41. Lee J, Son MJ, Woolard K, Donin NM, Li A, Cheng CH, et al. Epigenetic-mediated dysfunction of the bone morphogenetic protein pathway inhibits differentiation of glioblastoma-initiating cells. Cancer Cell 2008;13(1):69–80 doi 10.1016/j.ccr.2007.12.005. [PubMed: 18167341]

42. Yan G, Zhao H, Zhang Q, Zhou Y, Wu L, Lei J, et al. A RIPK3-PGE2 Circuit Mediates Myeloid-Derived Suppressor Cell-Potentiated Colorectal Carcinogenesis. Cancer research 2018;78(19):5586–99 doi 10.1158/0008-5472.can-17-3962. [PubMed: 30012671]

43. Hegde PS, Karanikas V, Evers S. The Where, the When, and the How of Immune Monitoring for Cancer Immunotherapies in the Era of Checkpoint Inhibition. Clin Cancer Res 2016;22(8):1865–74 doi 10.1158/1078-0432.ccr-15-1507. [PubMed: 27084740]

44. Bercovici N, Trautmann A. Revisiting the role of T cells in tumor regression. Oncoimmunology 2012;1(3):346–50 doi 10.4161/onci.18800. [PubMed: 22737611]

45. Terabe M, Matsui S, Park JM, Mamura M, Noben-Trauth N, Donaldson DD, et al. Transforming growth factor-β production and myeloid cells are an effector mechanism through which CD1d-restricted T cells block cytotoxic T lymphocyte-mediated tumor immunosurveillance: abrogation

prevents tumor recurrence. The Journal of experimental medicine 2003;198:1741–52. [PubMed: 14657224]

46. Liu CY, Wang YM, Wang CL, Feng PH, Ko HW, Liu YH, et al. Population alterations of L-arginase- and inducible nitric oxide synthase-expressed CD11b+/CD14⁻/CD15+/CD33+ myeloid-derived suppressor cells and CD8+ T lymphocytes in patients with advanced-stage non-small cell lung cancer. Journal of cancer research and clinical oncology 2010;136(1):35–45. [PubMed: 19572148]

47. Amarnath S, Mangus CW, Wang JC, Wei F, He A, Kapoor V, et al. The PDL1-PD1 axis converts human TH1 cells into regulatory T cells. Science translational medicine 2011;3(111):111ra20 doi 10.1126/scitranslmed.3003130.

48. Prima V, Kaliberova LN, Kaliberov S, Curiel DT, Kusmartsev S. COX2/mPGES1/PGE2 pathway regulates PD-L1 expression in tumor-associated macrophages and myeloid-derived suppressor cells. Proceedings of the National Academy of Sciences of the United States of America 2017;114(5):1117–22 doi 10.1073/pnas.1612920114. [PubMed: 28096371]

49. Gonzalez-Junca A, Driscoll K, Pellicciotta I, Du S, Lo CH, Roy R, et al. Autocrine TGFbeta is a Survival Factor for Monocytes and Drives Immunosuppressive Lineage Commitment. Cancer immunology research 2018 doi 10.1158/2326-6066.cir-18-0310.

50. Hearps AC, Martin GE, Angelovich TA, Cheng W-J, Maisa A, Landay AL, et al. Aging is associated with chronic innate immune activation and dysregulation of monocyte phenotype and function. Aging Cell 2012;11(5):867–75 doi doi:10.1111/j.1474-9726.2012.00851.x. [PubMed: 22708967]

51. Omene C, Wu J, Frenkel K. Caffeic Acid Phenethyl Ester (CAPE) derived from propolis, a honeybee product, inhibits growth of breast cancer stem cells. Investigational New Drugs 2011;1–10 doi 10.1007/s10637-011-9667-8. [PubMed: 19784550]

52. Wu J, Omene C, Karkoszka J, Bosland M, Eckard J, Klein CB, et al. Caffeic acid phenethyl ester (CAPE), derived from a honeybee product propolis, exhibits a diversity of anti-tumor effects in pre-clinical models of human breast cancer. Cancer letters 2011;308(1):43–53 doi 10.1016/j.canlet.2011.04.012. [PubMed: 21570765]

53. Sud'ina GF, Mirzoeva OK, Pushkareva MA, Korshunova GA, Sumbatyan NV, Varfolomeev SD. Caffeic acid phenethyl ester as a lipoxygenase inhibitor with antioxidant properties. FEBS letters 1993;329(1–2):21–4. [PubMed: 7689063]

54. Lehmann BD, Bauer JA, Chen X, Sanders ME, Chakravarthy AB, Shyr Y, et al. Identification of human triple-negative breast cancer subtypes and preclinical models for selection of targeted therapies. J Clin Invest 2011;121(7):2750–67 doi 10.1172/jci45014. [PubMed: 21633166]

55. UNSCEAR. Sources and effects of ionizing radiation New York: United Nations; 2006.

56. Krieglstein K, Miyazono K, ten Dijke P, Unsicker K. TGF-beta in aging and disease. Cell Tissue Res 2012;347(1):5–9 doi 10.1007/s00441-011-1278-3. [PubMed: 22183203]

57. Bianchi-Frias D, Vakar-Lopez F, Coleman IM, Plymate SR, Reed MJ, Nelson PS. The effects of aging on the molecular and cellular composition of the prostate microenvironment. PloS one 2010;5(9) doi 10.1371/journal.pone.0012501.

58. Wright EG, Coates PJ. Untargeted effects of ionizing radiation: Implications for radiation pathology. Mutation Res 2006;597(1–2):119–32. [PubMed: 16438994]

59. Hashemi Goradel N, Najafi M, Salehi E, Farhood B, Mortezaee K. Cyclooxygenase-2 in cancer: A review. Journal of cellular physiology 2019;234(5):5683–99 doi 10.1002/jcp.27411. [PubMed: 30341914]

60. Denkert C, von Minckwitz G, Darb-Esfahani S, Lederer B, Heppner BI, Weber KE, et al. Tumour-infiltrating lymphocytes and prognosis in different subtypes of breast cancer: a pooled analysis of 3771 patients treated with neoadjuvant therapy. The Lancet Oncology 2018;19(1):40–50 doi 10.1016/s1470-2045(17)30904-x. [PubMed: 29233559]

61. DeLong P, Tanaka T, Kruklitis R, Henry AC, Kapoor V, Kaiser LR, et al. Use of cyclooxygenase-2 inhibition to enhance the efficacy of immunotherapy. Cancer research 2003;63(22):7845–52. [PubMed: 14633712]
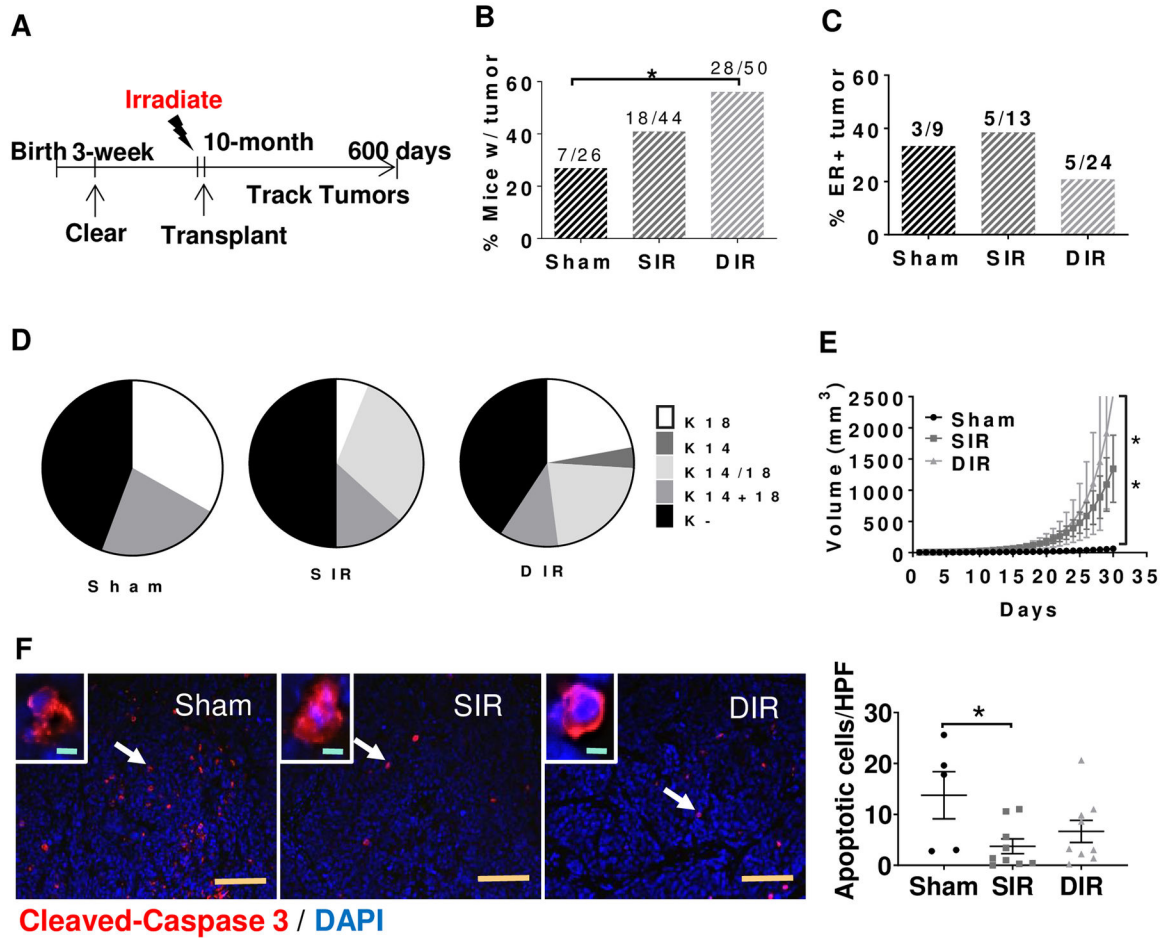
Figure 1. Tumor characteristics as a function of host irradiation at 10 months of age.
(A) Experimental scheme. The endogenous epithelium of the inguinal mammary glands of 3-week old mice were surgically removed. Mice were aged until 10 months-old, whole-body irradiated with SIR or DIR, and 3 days after irradiation subsequently transplanted with *Trp53*-null mammary fragments. Mice were monitored for tumorigenesis for approximately 600 days. (B) Frequency of tumors arising in aged hosts (corrected for outgrowth efficiency). $*p < 0.05$, Chi-square. Sparsely ionizing radiation (SIR); densely ionizing radiation (DIR). Numbers above columns represent mice with tumors over total mice in that group. (C) The frequency of ER–positive tumors as a function of aged host irradiation. Numbers above columns represent ER^+ tumors over total tumors in that group. (D) The keratin staining of tumors arising in sham-irradiated (n=9), SIR-irradiated (n=16), and DIR-irradiated (N=27) hosts. (E) Tumor growth rate over 30 days following detection by palpation for each group of aged mice. Mean±S.E.M. Sham: n=6; SIR: n=13; DIR: n=20. $**p < 0.01$. One-way ANOVA. (F) Left: Representative images of apoptotic cells marked by cleaved caspase 3. White arrows indicate zoomed cells in the image. Tan scale bars, 100 μm; Green scale bars, 5 μm. Right: Quantitation of apoptotic cell density in tumors arising in SIR (n=9) or DIR (n=9) irradiated hosts compared to tumors in sham group (n=5). Data are the mean±S.E.M.; $*p < 0.05$. Student t-test.
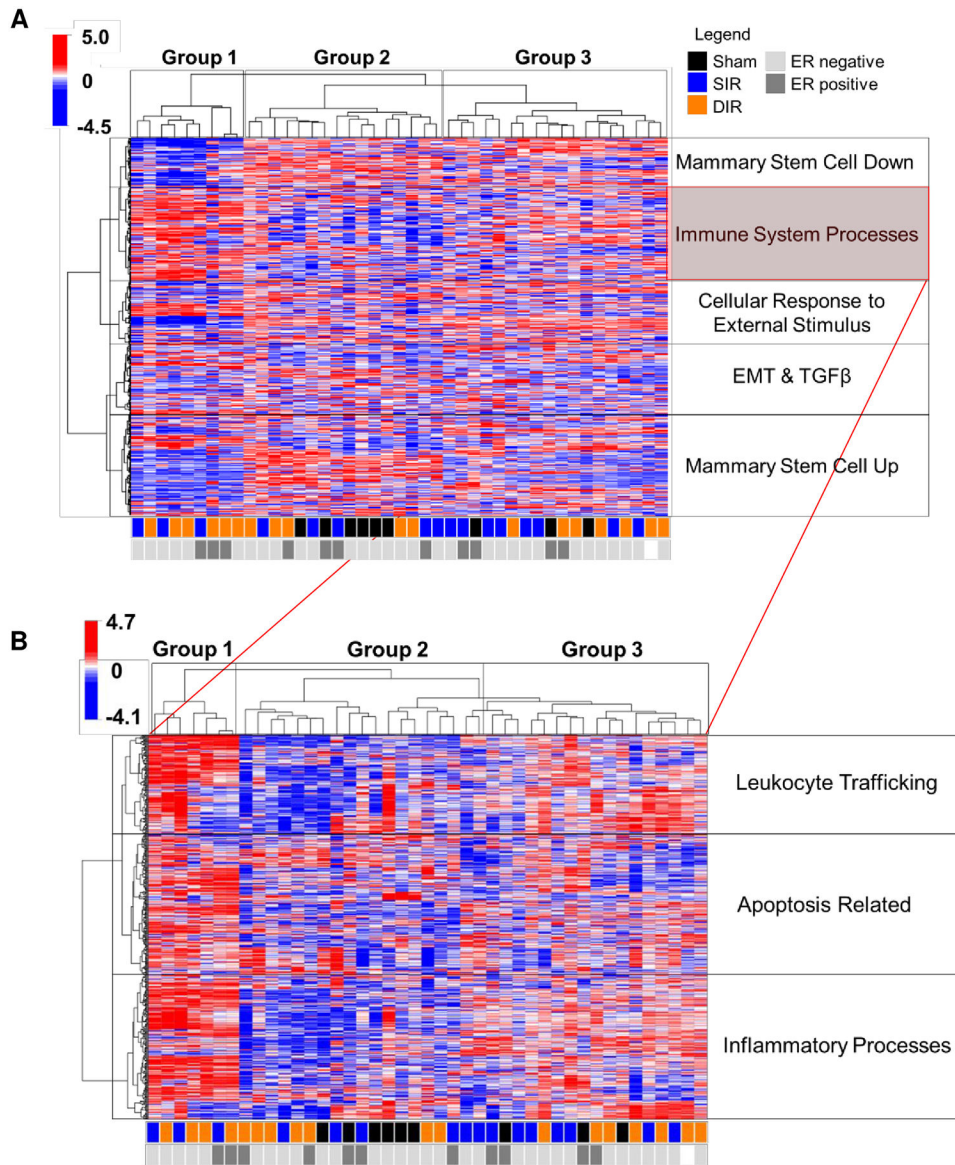
Figure 2. Tumors arising in aged, irradiated hosts evoke important programs implicated in immunity and inflammation.

(A) Unsupervised hierarchical clustering (UHC) of gene expression determined using an Affymetrix Genechip Mouse Gene 2.0 ST to profile 43 tumors (light grey ER−, n=32; dark grey ER+, n=11) arising in sham (black, n=9), SIR-irradiated (blue, n=15), and DIR-irradiated (orange, n=19) aged mice. 5 major gene clusters indicated. (B) Expression profiling of tumors arising in irradiated hosts. Enlarged view of gene cluster 2 (immune system processes) and the 3 indicated associated minor gene clusters.
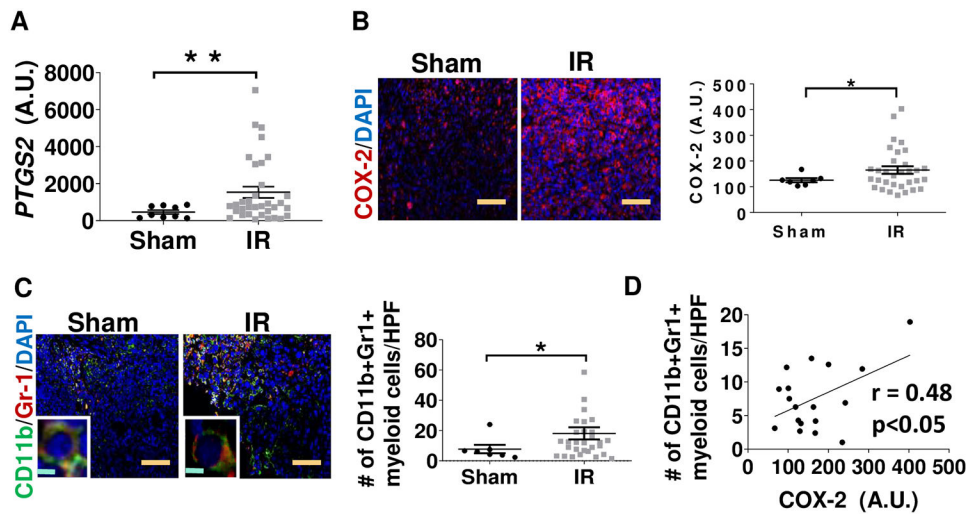
Figure 3. An immunosuppressive TME is prominent in tumors arising in irradiated mice.
(A) Expression of *PTGS2* (COX-2) measured by the Affymetrix Genechip Mouse 2.0ST platform. Sham: n=9; irradiated (IR): n=34. Data showed the mean±S.E.M.; P values were determined by Mann–Whitney test. **p<0.01. (B) Quantification of COX-2 expression by immunofluorescence staining with representative images. Sham: n=7; IR: n=32. *p<0.05 by Student t-test (bars, mean±S.E.M.). Tan scale bars, 100 μm. (C) Left: Representative images from immunofluorescence staining against CD11b and Gr1. Left down corners are zoomed positive cells in the image. Tan scale bars, 100 μm; Green scale bars, 5 μm. Right: Quantitation of CD11b⁺Gr1⁺ cells per HPF (Sham: n=7; IR: n=30) *p<0.05 by Student t-test (bars, mean±S.E.M.). (D) Correlation between CD11b⁺Gr1⁺ cells and COX-2 intensity per HPF. Each point is one tumor (n=18). p<0.05 was determined by PCC, r=0.48.
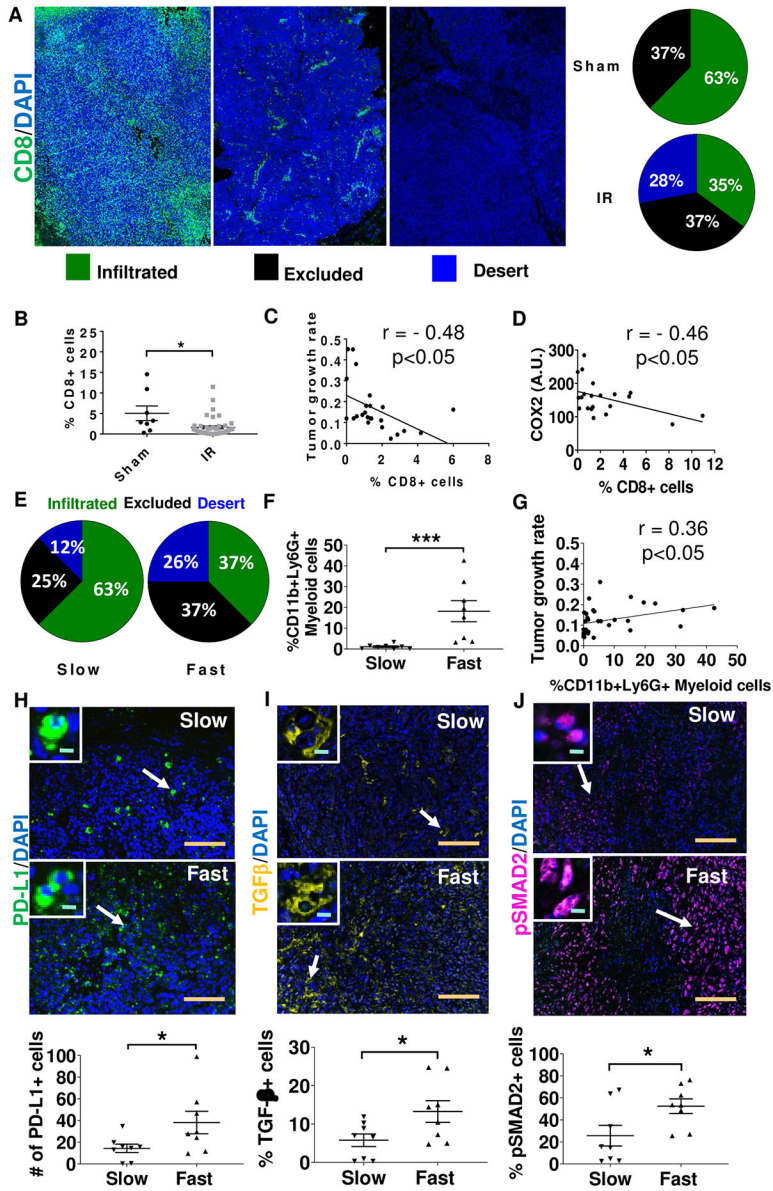
Figure 4. Patterns of CD8^{+} lymphocytic infiltration associate with tumor growth rate.
(A) Left: Representative images of *Trp*53-null mouse mammary gland tumors that were stained with anti-CD8 (green) and DAPI (blue) and scanned using the Vectra system. Right: Tumors were classified by 3 independent observers as inflamed (green), excluded (black), or desert (blue) as described in Methods. The proportion of tumor types as a function of host irradiation are shown for sham (n=8) and irradiated (IR, n=43) hosts. (B) The proportion of CD8^{+} cells within the tumor region of tumors from the sham (n=8) and IR groups (n=43). *p<0.05 by Mann Whitney test (bars, mean±S.E.M.). (C) Correlation between the proportion of CD8^{+} cells within the tumor region and tumor growth rate (n=24; Sham, n=4; IR, n=20). PCC r=−0.48, p<0.05. (D) Correlation between the proportion of CD8^{+} within the tumor region and COX-2 mean intensity. n=21; Sham, n=5; IR, n=16). PCC r=−0.46, p<0.05. (E) The immune infiltrate status of the bottom (i.e. slow, n=8) and top (i.e. fast, n=8)

quartile based on growth rate. Inflamed: green; Excluded: black; Desert: blue. (F) The proportion of CD11b$^+$Ly6G$^+$ myeloid cells within fast-growing tumors compared to slow-growing tumors. Slow, n=8; Fast, n=8. ***p<0.001, Mann Whitney test (bars, mean ±S.E.M.). (G) Correlation between the proportion of CD11b$^+$Ly6G$^+$ myeloid cells and tumor growth rate. n=19 (5 from Sham, 14 from IR). PCC r=0.36, p<0.05. (H) Top: Representative images of PD-L1 in slow- and fast-growing tumors. Bottom: Quantification of the frequency of PD-L1$^+$ cells in fast-growing tumors (n=8) compared to slow-growing tumors (n=8). *p<0.05, Mann Whitney test (bars, mean±S.E.M.). (I) Top: Representative images of TGFβ in slow- and fast-growing tumors. Bottom: Quantification of TGFβ$^+$ cells in fast-growing tumors vs. slow-growing tumors. *p<0.05, Mann Whitney test (bars, mean ±SEM). (J) Top: Representative images of pSMAD2 in slow- (n=8) and fast- (n=8) growing tumors. Bottom: Quantification of pSMAD2$^+$ cells in fast-growing tumors (n=8) than slow-growing tumors (n=8). *p<0.05, Mann Whitney test (bars, mean±SEM). For (H) to (J) images, white arrows indicate cells zoomed in the image. Tan scale bars, 100 µm; Green scale bars, 5 µm.
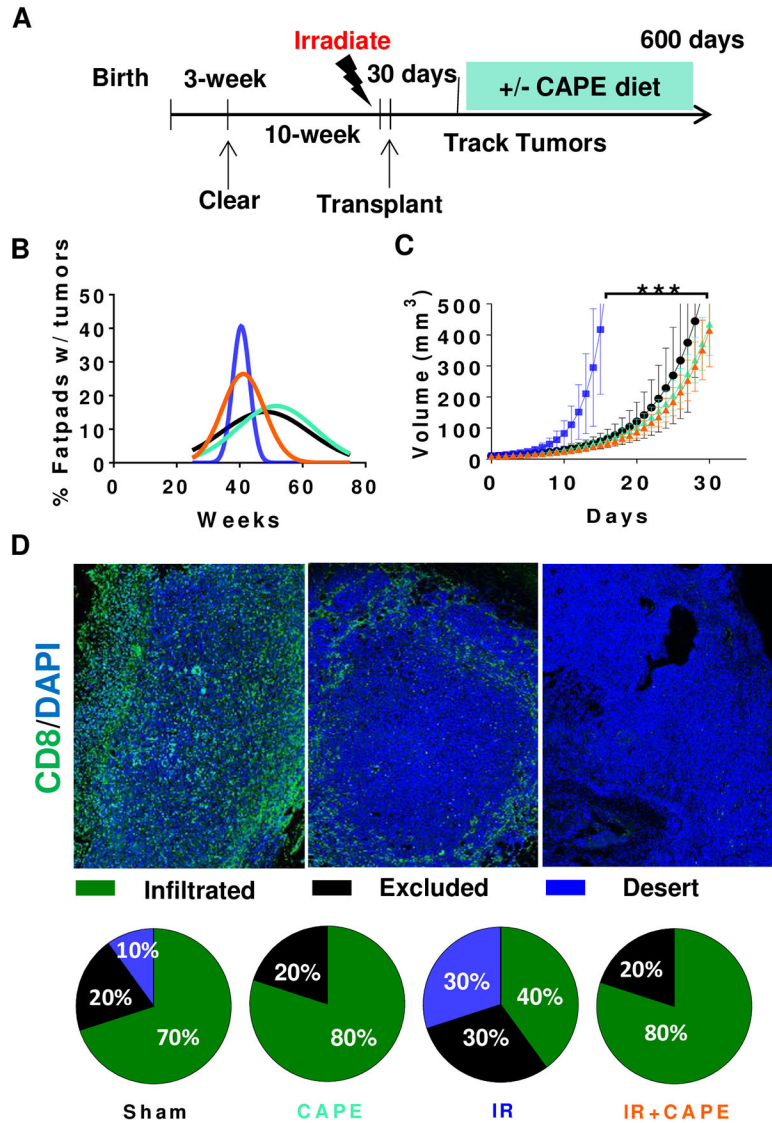
Figure 5. CAPE prevents aggressive tumors from developing in irradiated hosts.
(A) Experimental scheme. The endogenous epithelium of the inguinal mammary glands of 3-week old mice were surgically removed. Mice were aged until 10 weeks-old, whole-body irradiated with 100 cGY SIR, and subsequently transplanted 3 days after irradiation with *Trp53*-null mammary fragments. Some mice received CAPE in their diet beginning 4 weeks after transplantation. Mice were monitored for tumorigenesis for approximately 600 days. (B) Percentage of palpable tumors detected over time for each treatment group. Sham, n=25 (black solid line); CAPE only, n=23 (green); irradiated (IR) only, n=20 (dark blue); IR +CAPE, n=25 (Orange). (C) Tumor growth rate over 30 days for each treatment group. Mean±S.E.M.; Sham (black), n= 20; CAPE (green), n=20; IR (dark blue), n= 19; IR+CAPE (Orange), n= 22. ***p<0.001, One-way ANOVA. (D) Tumors were classified into three lymphocytic infiltration patterns based on CD8^{+} T-cell infiltrated (green), excluded (black), and desert (blue). IR (n=10), IR+CAPE (n=10), Sham (n=10), CAPE (n = 10).
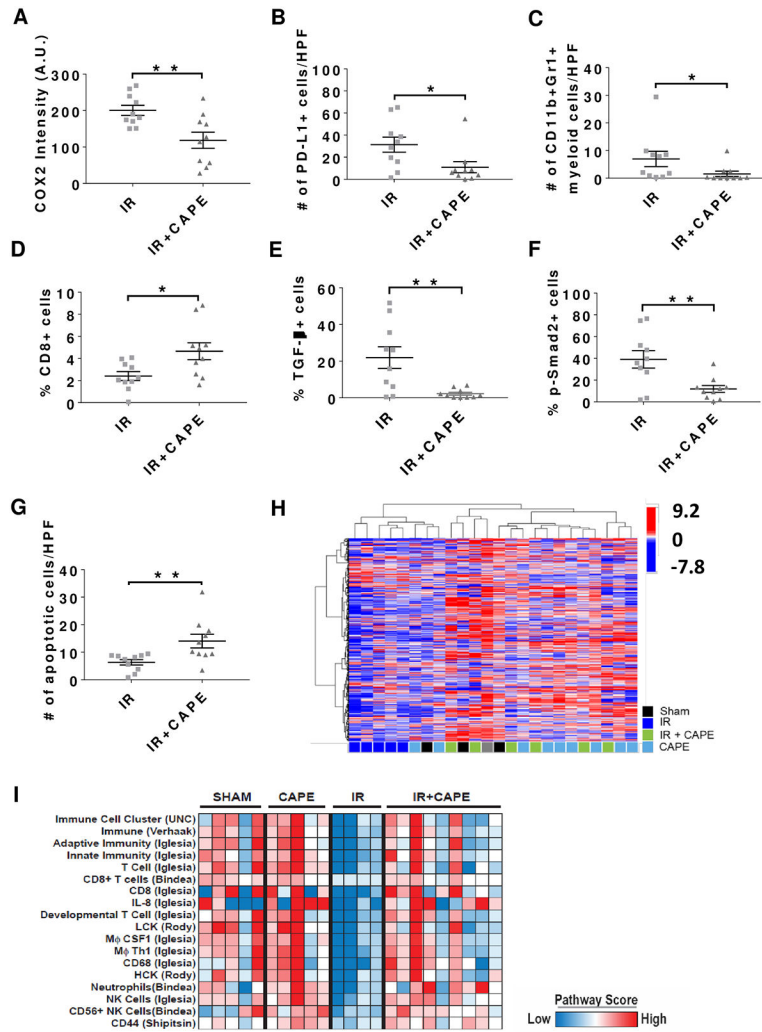
Figure 6. CAPE prevents establishment of an immunosuppressive TME.
(A-G) Immunofluorescence of tumors from irradiated (IR) and IR+CAPE groups were compared. (A) Quantification of COX-2 expression in tumors. (B) The number of PD-L1^{+} cells per high-powered field (HPF) in tumors. (C) The number of CD11b^{+}Gr1^{+} cells per HPF in tumors. (D) CD8^{+} T cells within the tumors. (E) TGFβ^{+} cells and (F) pSMAD2+ cells in tumors. (G) Cell apoptosis was marked by cleaved caspase-3^{+} cells per HPF in tumors. For (A-G), each point is a mean of five random images from one tumor, IR: n=10; IR+CAPE: n=10. *p<0.05; **p<0.01 by two-tail t-test or Mann Whitney test (bars, mean ±S.E.M.). (H) Heat map of differentially expressed immune genes. Sham (black, n=3), IR (dark blue, n=5), CAPE (light blue, n=9), CAPE+IR (green, n=6). (I) Panel of 18 gene expression signatures comparing tumors from sham, CAPE, IR, and IR + CAPE treatments; red indicates high signature score, whereas blue corresponds with low signature score.

Table 1:

Antibodies for Opal Staining

	1st Antibody	2nd Antibody	Opal dye
Set 1	Ly6G (60031, Stem Cell Tech)	Goat-anti-rat HRP (31470, Thermo Scientific)	Opal 520 (NEL796001KT, PerkinElmer)
Set 1	Foxp3 (1-5773-82, eBioscience)	Goat-anti-rat HRP (31470, Thermo Scientific)	Opal 540 (NEL796001KT, PerkinElmer)
Set 1	CD4 (14–9766, eBioscience)	Goat-anti-rat HRP (31470, Thermo Scientific)	Opal 570 (NEL796001KT, PerkinElmer)
Set 1	CD11b (ab133357, abcam)	Goat-anti-rabbit HRP (31466, Invitrogen)	Opal 620 (NEL796001KT, PerkinElmer)
Set 1	CD45 (ab10588, abcam)	Goat-anti-rabbit HRP (31466, Invitrogen)	Opal 690 (NEL796001KT, PerkinElmer)
Set 1	DAPI		Spectrum DAPI (NEL796001KT, PerkinElmer)
Set 2	CD8 (ab203035, abcam)	Goat-anti-rabbit HRP (31466, Invitrogen)	Opal 520 (NEL796001KT, PerkinElmer)
Set 2	Ki67 (RM9106-S1, ThermoFisher)	Goat-anti-rabbit HRP (31466, Invitrogen)	Opal 540 (NEL796001KT, PerkinElmer)
Set 2	CD4 (14–9766, eBioscience)	Goat-anti-rat HRP (31470, Thermo Scientific)	Opal 570 (NEL796001KT, PerkinElmer)
Set 2	CD3 (MA514524, ThermoFisher)	Goat-anti-rabbit HRP (31466, Invitrogen)	Opal 620 (NEL796001KT, PerkinElmer)
Set 2	Pan-Cytokeratin (ab9377, abcam)	Goat-anti-rabbit HRP (31466, Invitrogen)	Opal 690 (NEL796001KT, PerkinElmer)
Set 2	DAPI		Spectrum DAPI (NEL796001KT, PerkinElmer)
Set 3	Gr1 (RB6-8C5) (ab25377, abcam)	Goat-anti-rat HRP (31470, Thermo Scientific)	Opal 520 (NEL811001KT, PerkinElmer)
Set 3	p-SMAD2 (44–244G, ThermoFisher)	Goat-anti-rabbit HRP (31466, Invitrogen)	Opal 540 (NEL811001KT, PerkinElmer)
Set 3	TGF-β (AF-101-NA, R&D system)	Goat-anti-Chicken HRP (ab6877, abcam)	Opal 570 (NEL811001KT, PerkinElmer)
Set 3	CD8 (ab203035, abcam)	Goat-anti-rabbit HRP (31466, Invitrogen)	Opal 620 (NEL811001KT, PerkinElmer)
Set 3	CD11b (ab133357, abcam)	Goat-anti-rabbit HRP (31466, Invitrogen)	Opal 650 (NEL811001KT, PerkinElmer)
Set 3	Pan-Cytokeratin (ab9377, abcam)	Goat-anti-rabbit HRP (31466, Invitrogen)	Opal 690 (NEL811001KT, PerkinElmer)
Set 3	DAPI		Spectrum DAPI (NEL811001KT, PerkinElmer)
Set 4	CD33 (NBP2–37388, Novus)	Opal Polymer HRP Ms+Rb (ARH1001EA, PerkinElmer)	Opal 520 (NEL811001KT, PerkinElmer)
Set 4	p-SMAD2 (44–244G, ThermoFisher)	Goat-anti-rabbit HRP (31466, Invitrogen)	Opal 540 (NEL811001KT, PerkinElmer)
Set 4	TGF-b 1D11 (BP0057, BioXcell)	Goat-anti-Ms IgG1 HRP (ab97240, abcam)	Opal 570 (NEL811001KT, PerkinElmer)
Set 4	CD11b (ab133357, abcam)	Goat-anti-rabbit HRP (31466, Invitrogen)	Opal 620 (NEL811001KT, PerkinElmer)
Set 4	COX2 (ab15191, abcam)	Goat-anti-rabbit HRP (31466, Invitrogen)	Opal 650 (NEL811001KT, PerkinElmer)
Set 4	PD-L1 (ab20592, abcam)	Goat-anti-rabbit HRP (31466, Invitrogen)	Opal 690 (NEL811001KT, PerkinElmer)
Set 4	DAPI		Spectrum DAPI (NEL811001KT, PerkinElmer)